www.advintellsyst.com

# Deep-Learning Model for Central Nervous System Infection Diagnosis and Prognosis Using Label-Free 3D Immune-Cell Morphology in the Cerebrospinal Fluid

Bo Kyu Choi, Ho Heon Yang, Jong Hyun Kim, JaeSeong Hong, Kyung Min Kim,\* and Yu Rang Park\*

Early diagnosis and prognostication of a central nervous system (CNS) infection is essential. This study aims to use immune-cell morphology to develop a deeplearning model for this purpose. Overall, 1427 3D images of cerebrospinal fluid (CSF) immune cells from 14 patients with CNS infections are obtained using holotomography. The images are categorized into infection etiology groups (viral and non-viral) and prognosis groups (based on the modified Rankin Scale score at discharge). A deep-learning model is constructed to predict the etiology and prognosis of CNS infections using the immune-cell morphology. Cell morphological features and spatial distribution of CSF immune cells differ significantly between patients in the viral and nonviral groups and between prognosis groups. The model yields areas under the receiver operating characteristic curve of 0.89 and 0.79 for the diagnosis and prognosis, respectively. As more cell images are used, the prediction and model robustness improve. With <10 cells, both tasks exhibit a nearly 100% predictive performance. After dividing the cells into eight shells, significant refractive index variations are observed. This is the first study to use CSF cell morphology for the diagnosis and prognostication of CSF infections. These findings can help improve patient outcomes.

1. Introduction

Infections affecting the membranes and tissues of the central nervous system (CNS) are associated with high mortality rates and long-lasting impairment, highlighting the need for improved diagnostic and therapeutic methods. <sup>[1]</sup> The etiological spectrum of CNS infections includes viruses, bacteria, mycobacteria, fungi, and parasites; consequently, accurate diagnosis and effective treatment remain a challenge, often resulting in poor outcomes. <sup>[2]</sup> The pathogen is confirmed through culture and antibody test results,

which require time and specialized equipment and facilities.<sup>[3]</sup> Hence, the information gleaned from clinical observations can be used to deduce the underlying etiology.<sup>[4]</sup>

The cerebrospinal fluid (CSF) surrounds the brain and spinal cord, providing cushioning and protection. It helps maintain a stable CNS environment. In cases of inflammation within the CNS, an increase in the number of immune cells and alterations in the CSF may occur, helping identify the cause of an infection in the clinical practice. [4,5] Morphological alterations in blood immune cells occur quickly with inflammation, reflecting the immunological response of the patient and helping identify the underlying pathology. [6,7] While recent studies have used genomic analysis of the CSF immune cells to elucidate the inflammatory response, to the best of our knowledge, no quantitative studies have been conducted on the morphological changes in these immune cells.[8,9]

We explored the potential of immune-cell morphologies as biomarkers for CNS infections in human CSF samples using deep-learning technology. Conventional staining and fixation methods have limitations, as they can distort the natural state of cells and hinder dynamic cellular studies. Therefore, we captured 3D images of the CSF immune cells using holotomography, which can generate label-free 3D images of live cells, and quantify a measurable physical parameter, the refractive index (RI), associated with cellular biochemical and biophysical characteristics. [10–12] Finally, label-free 3D imaging was used

B. K. Choi, H. H. Yang, J. H. Kim, J. S. Hong, Y. R. Park Department of Biomedical Systems Informatics Yonsei University College of Medicine Seoul 03722, Korea E-mail: yurangpark@yuhs.ac

The ORCID identification number(s) for the author(s) of this article can be found under https://doi.org/10.1002/aisy.202401145.

© 2025 The Author(s). Advanced Intelligent Systems published by Wiley-VCH GmbH. This is an open access article under the terms of the Creative Commons Attribution License, which permits use, distribution and reproduction in any medium, provided the original work is properly cited.

DOI: 10.1002/aisy.202401145

B. K. Choi Department of Neurology Gangnam Severance Hospital Yonsei University College of Medicine Seoul 06273, Korea

J. H. Kim LG AI Research Seoul 07789, Korea

K. M. Kim
Department of Neurology
Yonsei University College of Medicine
Seoul 03722, Korea
E-mail: penlighting11@yuhs.ac



ADVANCED Intelligent Systems

www.advancedsciencenews.com www.advintellsyst.com

to quantitatively evaluate immune-cell structural changes in the CSF of patients with CNS infections.

### 2. Results

#### 2.1. Study Design and Patient Enrollment

We performed a prospective cohort study between January and October 2022 at Severance Hospital in Seoul, Republic of Korea. Patients who met the following inclusion criteria were enrolled: 1) presenting with fever, headache, and other neurological abnormalities prompting clinical suspicion of encephalitis or meningitis; 2) >10 cells  $\mu L^{-1}$  in the CSF sample; and 3) age >18 years. Between January and October 2022, 14 patients with CNS infections were enrolled in this study; 1427 3D images of immune cells within their CSF were included. The cohort consisted of nine patients with viral infections, four with bacterial infections, and one with tuberculosis. The modified Rankin Scale (mRS) score at discharge was used for prognostic assessment, and, three patients exhibited poor prognosis (mRS score >4 at discharge). The mRS score is a regularly used measure for assessing dependent or disabled people, who have experienced a stroke or other neurological disabilities, in their ability to perform everyday activities. [13] The differences in clinical features between patients with and without viral infections are shown in Table 1. Compared to patients with viral infection, those with infections of other etiologies showed higher CSF white blood cell counts and protein levels. In addition, blood procalcitonin and Creactive protein levels, which are commonly used as inflammatory biomarkers, tended to be elevated in patients with nonviral pathogens.

In each patient, immune cells were extracted from the CSF samples obtained by lumbar puncture (Figure 1A). Subsequently, 3D images of the immune cells were captured using holotomography. We extracted biophysical features such as protein density and dry mass and analyzed the spatial distribution of the internal cell components based on their RI values (Figure 1B). Labels pertaining to the etiology and prognosis of each patient's infection were assigned to each image. The labels for pathogens were determined based on information recorded by physicians in the electronic medical records. We developed a deep-learning model for causal and prognostic prediction (Figure 1C). After dichotomizing patients based on the cause of the infection, we further subdivided the sample and conducted a classification task. We validated this model by analyzing quantitative information on cellular morphology and clinical data from each patient. Additionally, we ensured the explainability of the artificial intelligence (AI) model.

# 2.2. Cell Morphological Differences Between the Groups

Adv. Intell. Syst. 2025, 7, 2401145

We also examined differences in 3D cell morphology between the etiological and prognostic groups. Quantitative metrics were extracted from the 3D images of the cells and compared across each group (Figure S1, Supporting Information). The protein density of the CSF immune cells in patients with viral infections was significantly higher than that in the other groups (p < 0.001), and the mean whole-cell refractive index (RI) value differed

between the groups defined by the cause of infection (Figure S1A–C, Supporting Information). Quantitative metrics of the cells were compared between the two groups with different prognoses, and all of them showed statistically significant differences between the two groups (Figure S1D–F, Supporting Information). Immune cells in the group with poor prognosis generally exhibited higher dry mass and lower protein density. Furthermore, the mean values of the overall RI were significantly different between the good and poor prognosis groups.

#### 2.3. Model Performance

We used the modified DenseNet architecture (Figure S2, Supporting Information) for the deep learning process to classify patients based on their infection etiology and predict their prognoses. By utilizing 3D images of the CSF immune cells, our deep-learning model achieved an area under the receiver operating characteristic curve (AUROC) of 0.89 (95% confidence interval [CI] 0.88-0.91) in distinguishing patients with viral infections from those with other etiologies (Figure 2A). We randomly sampled cell images to assess the predictive performance and observed a significant increase in AUROC as the number of cells used increased (Figure 2B). We achieved an AUROC of 0.99, demonstrating nearly 100% predictive power, using only five cells, and surpassing the performance of the previous models. As the number of cells used increased, we observed a reduction in the AUROC range, indicating that selecting more cells reduced the impact of selection bias and variance. We also verified the improved robustness of our model using this result. After subdividing the "other pathogens" group into bacterial and tubercular, multiclassification was performed. Even in this scenario, the model yielded an AUROC of 0.86 (Figure S3, Supporting Information). We conducted a subgrouping of three viruses belonging to the Herpesviridae family commonly observed in CNS viral infections (herpes simplex virus type 1, varicella-zoster virus, and human herpesvirus 6) and performed multiclassification. We observed the ability of our model to classify infections caused by each virus within the same family with an AUROC of 0.87 (Figure S4, Supporting Information). We also performed the same task with the ResNet-101-based model to compare the performance of our presented model with the widely known models. In the classification task, the performance of the ResNet-based model was measured at AUROC 0.82, lower than that of our model (Figure S5, Supporting Information).

The mRS score is commonly used for a prognostic evaluation of neurological disorders, and a score of 4 is defined as moderately severe disability, where the individual is unable to walk without assistance and requires help for basic bodily needs. In this study, we defined the poor prognosis group as patients with mRS scores of  $\geq$ 4 at discharge. Our model predicted patient outcomes with 3D images of CSF immune cells and achieved a performance AUROC of 0.79 (95% CI 0.77–0.81) (Figure 2C). During prognosis prediction, we also conducted random sampling of 3D cell images and checked an AUROC for each number of cells (Figure 2D). Similarly, we observed a significant improvement in the predictive performance with an increasing number of cells. For prognostic prediction, the extraction of five cells resulted in an AUROC of 0.94, indicating high predictive power.

ADVANCED INTELLIGENT SYSTEMS

www.advancedsciencenews.com www.advintellsyst.com

Table 1. Clinical feature distribution for each etiology.

Etiologies <sup>a)</sup>	Total [n = 14]	Virus [ <i>n</i> = 9]	Others $[n=5]$
Number of cell images	1427	748	679
Age	60.5 (37, 66)	43 (37, 62)	67 (66, 67)
Female sex	8 (57.1%)	5 (55.6%)	3 (60.0%)
Body mass index	22.3 (20.5, 23.6)	21.5 (19.6, 22.7)	23.4 (22.1, 23.6)
Comorbidities			
Charlson comorbidity index	2.5 (0, 5)	2 (0, 3)	5 (5, 6)
Tuberculosis history	1 (7.1%)	0 (0.0%)	1 (20.0%)
Seizure	2 (14.3%)	1 (11.1%)	1 (20.0%)
Abnormal brain CT	4 (28.6%)	1 (11.1%)	3 (60.0%)
Abnormal chest X-ray	2 (14.3%)	2 (22.2%)	0 (0.0%)
EEG			
Abnormal	5 (35.7%)	2 (22.2%)	3 (60.0%)
Unreactivity	0 (0.0%)	0 (0.0%)	0 (0.0%)
Slowing	5 (35.7%)	2 (22.2%)	3 (60.0%)
Epileptiform discharges	1 (7.1%)	1 (11.1%)	0 (0.0%)
Clinical severity			
Modified Rankin Scale at discharge	0 (0, 2)	0 (0, 1)	0 (0, 5)
In hospital mortality	1 (7.1%)	0 (0.0%)	1 (20.0%)
ICU admission during hospitalization	4 (28.6%)	1 (11.1%)	3 (60.0%)
ICU duration [days]	0 (0, 3)	0 (0, 0)	3 (0, 3)
Length of stay [days]	15.5 (8, 43)	9 (7, 16)	43 (22, 52)
Abnormal mentality at day 1 [n, %]	6 (42.9%)	2 (22.2%)	4 (80.0%)
Glasgow Coma Scale on day 1	15 (14, 15)	15 (15, 15)	14 (13, 14)
Vital signs			
Mean systolic blood pressure [mmHg]	125.8 (113.3, 138.2)	125.1 (113.3, 137.3)	133.6 (120.4, 143.1)
Mean diastolic blood pressure [mmHg]	71.1 (62.9, 81.1)	75.0 (70.7, 84.7)	68.6 (62.9, 69.4)
Mean heart rate [rate min <sup>-1</sup> ]	79.8 (77.9, 89.3)	78.5 (74.8, 88.3)	85.8 (80.0, 103.4)
Mean respiratory rate [rate min-1]	18.5 (18.0, 19.3)	18.3 (17.2, 18.5)	18.6 (18.5, 19.6)
Maximum body temperature [°C]	38.0 (37.6, 38.3)	38.0 (37.4, 38.2)	37.9 (37.9, 39.1)
Mean body temperature [°C]	37.2 (37.1, 37.3)	37.2 (37.1, 37.3)	37.1 (36.9, 37.2)
CSF			
WBC count [/μL]	87.5 (43.0, 170.0)	58.0 (28.0, 75.0)	170.0 (137.0, 900.0)
Protein [mg dL <sup>-1</sup> ]	82.2 (63.2, 118.9)	72.7 (54.6, 88.0)	118.9 (103.6, 149.4)
Glucose [mg $dL^{-1}$ ]	65.0 (48.0, 75.0)	63.0 (47.0, 73.0)	73.0 (48.0, 76.0)
CSF/serum glucose ratio	0.6 (0.5, 0.7)	0.7 (0.6, 0.7)	0.5 (0.5, 0.5)
RBC count $> 100\mu L^{-1}$	4 (28.6%)	1 (11.1%)	3 (60.0%)
Turbidity	3 (21.4%)	1 (11.1%)	2 (40.0%)
Adenosine deaminase [IU L <sup>-1</sup> ]	2.3 (2.1, 4.8)	2.3 (2.2, 2.8)	5.2 (1.4, 6.6)
Abnormal color	2 (14.3%)	0 (0.0%)	2 (40.0%)
High pH	13 (92.9%)	1 (11.1%)	3 (60.0%)
Blood			
WBC count $[10^9 L^{-1}]$	7.8 (5.9, 9.2)	8.2 (6.4, 9.2)	7.3 (5.7, 8.9)
Hemoglobin $[g dL^{-1}]$	12.8 (12.2, 13.7)	12.8 (12.2, 13.0)	13.7 (12.7, 14.4)
Platelet count $[10^9 L^{-1}]$	234.5 (200.0, 285.0)	235.0 (211.0, 285.0)	234.0 (105.0, 244.0)
Mean platelet volume [fL]	9.4 (8.8, 10.4)	9.5 (9.0, 10.4)	8.8 (8.4, 11.2)
Red cell distribution width [%]	13.4 (12.7, 13.8)	12.7 (12.6, 13.7)	13.6 (13.2, 13.8)
Delta neutrophil index [%]	0.0 (0.0, 0.0)	0.0 (0.0, 0.0)	0.0 (0.0, 0.0)

ADVANCED INTELLIGENT SYSTEMS

www.advancedsciencenews.com www.advintellsyst.com

Table 1. Continued.

Etiologies <sup>a)</sup>	Total $[n=14]$	Virus [ <i>n</i> = 9]	Others $[n=5]$
Prothrombin time [INR]	0.9 (0.9, 1.1)	0.9 (0.9, 0.9)	1.2 (1.0, 1.2)
aPTT [s]	32.2 (26.2, 34.5)	32.6 (25.9, 34.5)	31.9 (30.7, 33.6)
Sodium ion concentration $[mmol L^{-1}]$	136.5 (135.0, 139.0)	138.0 (135.0, 139.0)	136.0 (134.0, 137.0)
Potassium ion concentration [mmol $L^{-1}$ ]	4.0 (3.9, 4.3)	4.1 (3.9, 4.3)	4.0 (3.6, 4.2)
$tCO2 [mmol L^{-1}]$	27.0 (26.0, 27.5)	27.0 (27.0, 28.0)	26.0 (26.0, 26.0)
Blood urea nitrogen [mg dL <sup>-1</sup> ]	16.5 (10.3, 22.5)	11.1 (9.7, 16.6)	22.5 (22.1, 22.5)
Creatinine [ $mg dL^{-1}$ ]	0.7 (0.6, 0.8)	0.7 (0.6, 0.8)	0.7 (0.6, 0.8)
Glucose [mg $dL^{-1}$ ]	134.5 (102.0, 158.0)	128.0 (94.0, 158.0)	138.0 (137.0, 153.0)
Albumin $[g dL^{-1}]$	4.2 (3.8, 4.6)	4.3 (4.1, 4.6)	3.8 (3.7, 4.1)
Aspartate transaminase [IU $L^{-1}$ ]	26.5 (17.0, 57.0)	21.0 (13.0, 30.0)	36.0 (25.0, 57.0)
Alanine aminotransferase [IU L <sup>-1</sup> ]	19.0 (14.0, 51.0)	17.0 (13.0, 21.0)	32.0 (19.0, 73.0)
Total bilirubin [mg dL <sup>-1</sup> ]	0.8 (0.5, 1.2)	0.5 (0.4, 1.0)	1.2 (0.9, 1.5)
Alkaline phosphatase [IU $L^{-1}$ ]	84.0 (65.0, 99.0)	68.0 (62.0, 85.0)	99.0 (87.0, 103.0)
Uric acid $[mg dL^{-1}]$	4.1 (2.6, 5.1)	4.2 (3.4, 5.1)	3.2 (2.6, 4.8)
Inorganic phosphorus [mg dL <sup>-1</sup> ]	3.3 (2.9, 3.5)	3.4 (3.2, 3.5)	2.9 (2.2, 3.1)
Calcium [ $mg dL^{-1}$ ]	9.0 (8.4, 9.2)	9.0 (8.9, 9.2)	8.9 (8.3, 9.0)
Creatinine kinase [IU L-1]	121.0 (29.0, 270.0)	29.0 (25.5, 75.0)	1701.5 (270.0, 3133.0)
Ammonia [ $\mu g dL^{-1}$ ]	54.0 (33.0, 59.0)	54.0 (43.5, 56.5)	54.5 (22.0, 87.0)
C-reactive protein [mg L <sup>-1</sup> ]	4.0 (0.6, 6.9)	1.7 (0.3, 5.2)	6.9 (4.1, 61.8)
Erythrocyte sedimentation rate $[mm  h^{-1}]$	12.0 (4.0, 21.0)	10.0 (4.0, 12.0)	17.5 (8.5, 38.0)
Procalcitonin [ng mL <sup>-1</sup> ]	0.1 (0.0, 0.2)	0.0 (0.0, 0.1)	0.1 (0.1, 2.1)
Lactate [mmol L <sup>-1</sup> ]	2.5 (2.0, 3.1)	2.2 (1.8, 2.7)	4.2 (3.1, 5.1)

a) One-way analysis of variance was used to compare continuous variables, and chi-square test was used to compare categorical variables. Abbreviations: CT, computed tomography; EEG, electroencephalography; CSF, cerebrospinal fluid; WBC, white blood cell; RBC, red blood cell; aPTT, activated partial thromboplastin time

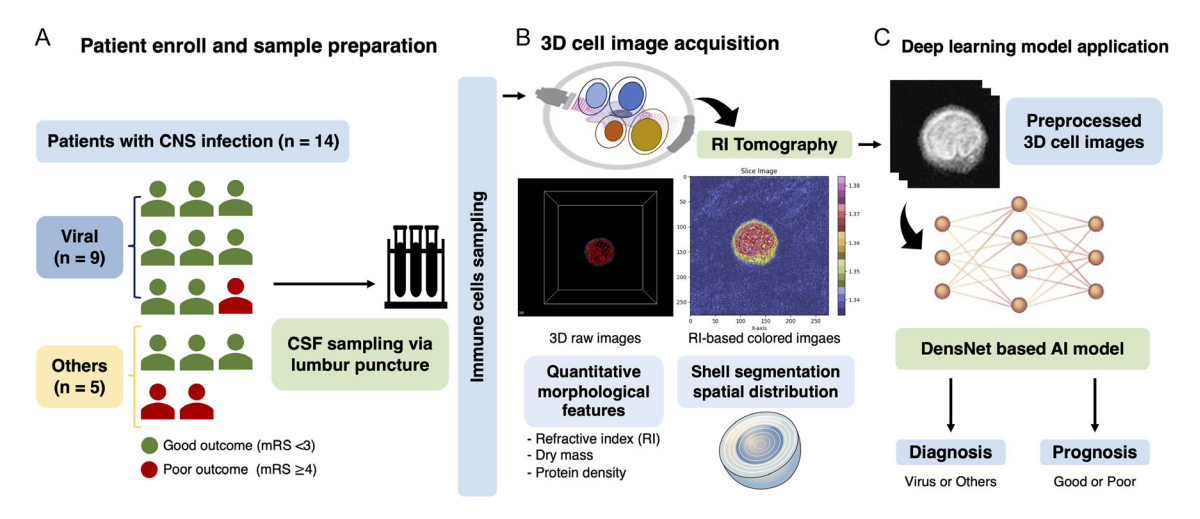


Figure 1. Schematic overview of the study workflow: A) This study included 14 patients with a CNS infection, including nine patients with a viral infection. Patients were divided into two prognosis groups based on the modified Rankin Scale (mRS) score at discharge, with a cutoff of 4 points. Three patients were classified into the poor prognosis group. CSF samples were collected from all patients via a lumbar puncture; only the cellular layer was isolated from the samples. B) 3D cell images were acquired using holotomography. The quantitative morphological features were also obtained and compared. All images underwent a preprocessing step before being used in the deep-learning model. C) Deep-learning models, based on the DenseNet model for CNS infection diagnosis and prognostication, were developed and validated based on internal cell structure.

conditions) on Wiley Online Library for rules of use; OA articles are governed by the applicable Creative Commons License

www.advancedsciencenews.com

SYSTEMS

www.advintellsyst.com

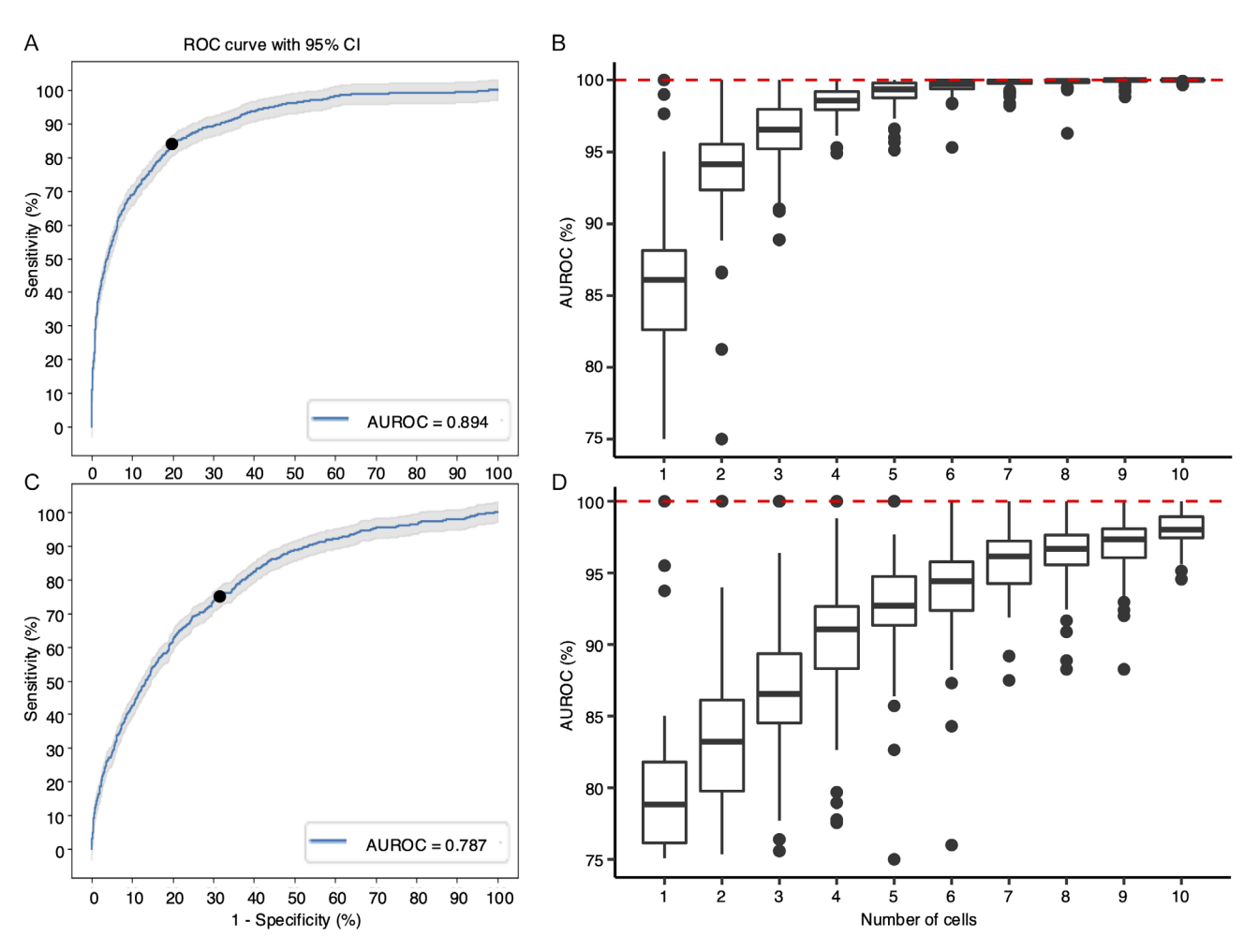


Figure 2. AUROC for the deep-learning models developed in the study: A) Receiver operating characteristic (ROC) curve with the corresponding 95% CI in predicting the etiology of the CNS infection. The black dot depicts the best point of the curve. B) Boxplot of AUROCs for predicting infection etiology when cells were randomly sampled. C) ROC curve with the corresponding 95% CI in predicting the etiology of the CNS infection. The black dot depicts the best point of the curve. D) Boxplot of AUROC curves for predicting the prognostic group when cells were randomly sampled.

While it is challenging to make a direct comparison owing to the differences in conditions from previous studies predicting outcomes in CNS infections, it is evident that our model demonstrated high predictive power, even when considering this aspect. As the number of cells increased, the variability in AUROC decreased (Figure 2D).

#### 2.4. Interpretability and Explainability of AI Models

In patients with a viral infection (**Figure 3A**), a decrease in the density of a cell component appeared more centrally, which explains why the effective cell region was limited to the inner shell. In shells 6, 7, and 8, there was a significant difference between the groups (p < 0.001). In contrast, in the case of nuclear component density (Figure 3B), the proportion of nuclear components in the viral group representing high RI values was higher for all shells than for the other groups, and the nuclear components were evenly lateral. This observation led us to infer that the proportion of nuclear components in

the cells of patients with viral infections was larger than that in the cells of other groups, and the size of the effective nucleus, defined as containing nuclear components, was also larger. Overall, patients with viral infections have a small effective cell size but a large effective nucleus size, and the nucleus is a major component of the cell. Figure 3C,D shows the spatial density distribution in patient groups based on their prognosis; the size of the effective cells was smaller and that of the more effective nucleus was wider in patients with good outcomes than in their counterparts.

We used the gradient-weighted class activation mapping (Grad-CAM) algorithm to explain the deep-learning models. Figure 3E depicts the intracellular region that the deep-learning model localizes, suggesting that the classification task is performed based on the proper extraction of morphological features from the RI distribution in the immune cell, especially the morphological distribution of the nucleus. We also observed that even during prognosis prediction using Grad-CAM, it was possible to utilize differences within cells for prediction (Figure 3F).

onditions) on Wiley Online Library for rules of use; OA articles are governed by the applicable Creative Commons License

ÎNTELLIGENT SYST<u>ems</u>

www.advancedsciencenews.com www.advintellsyst.com

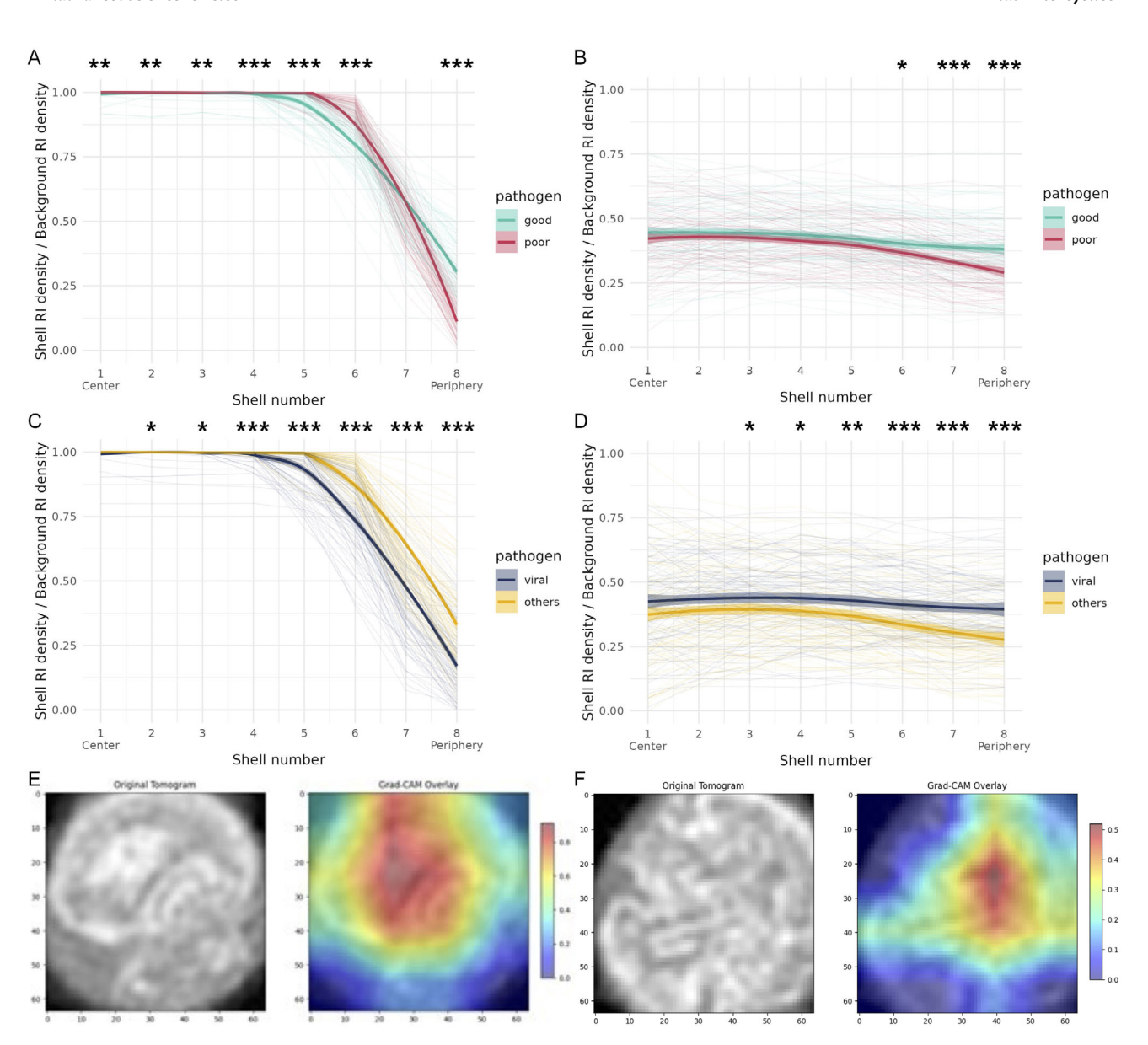


Figure 3. Spatial distribution within cells for each pathogen and prognosis group, and validation of the morphological feature through the visual explanation: A–D) 2D sectioned images are divided into eight elliptically shaped regions, with the region closest to the center referred to as shell 1 and the region furthest from the center referred to as shell 8. The shell density is defined as the ratio of pixels with a value above the target RI to the total number of pixels in that shell. The shell density of (A) the overall RI and (B) the nuclear component RI of each pathogen group are demonstrated. The shell density of (C) the overall RI and (D) the nuclear component RI of each prognostic group are compared. The gradient-weighted class activation mapping (Grad-CAM) algorithm is used to visually expand the presented deep-learning models. The Grad-CAM images superimposed on the original image are plotted in panels E) (etiological prediction) and F) (prognostic prediction).

#### 3. Discussion

In this study, we identified the causal pathogen and predicted the prognosis of patients with CNS infections, based on 3D images of the CSF immune cells, using a deep-learning model. To the best of our knowledge, this is the first study to utilize the morphological features of CSF cells for this purpose. We believe that this model may help reduce the time required for patient diagnosis and prognostication. Furthermore, we report how classification using the deep-learning model was achieved using various

methods. This study demonstrated that 3D label-free CSF immune-cell morphology could be a potential biomarker for CNS infections.

Early diagnosis and treatment of CNS infections are crucial.<sup>[1]</sup> However, in real-world clinical settings, they are difficult to achieve. Previous studies have commonly relied on the CSF test results to identify the cause. Manual confirmation of cell shape and count are required when using conventional methods to identify cells. This process relies heavily on human labor, and observer expertise can affect the results. [14]

ADVANCED INTELLIGENT SYSTEMS

www.advancedsciencenews.com www.advintellsyst.com

The equipment for measuring the glucose and protein levels also takes over 3 h to generate results. [15] However, our deep-learning model, which utilizes 3D images of immune cells in the CSF, can significantly reduce the time taken from CSF collection to evaluation to within 1 h. The method we propose is faster than the current diagnostic techniques, such as brain imaging, and the frequently employed clinical biomarkers such as blood levels of procalcitonin and C-reactive protein. [16–20] In previous studies, clinical indicators were collected for predictive analysis using AI, which demonstrated performance accuracy of >90%. [19,21] These studies primarily relied on electronic medical records data, which may introduce delays in data input and availability. In addition, the accuracy of the predictions can be influenced by the person entering the data. Furthermore, a common limitation across most studies was the collection of variables at least 24 h postadmission before constructing predictive models. In contrast, our approach, which used <10 CSF immune cell images, had an average AUROC value of 100% for both CNS infection diagnosis and prognosis prediction. In addition, as emphasized earlier, data collection and imaging can be performed within a very short timeframe after admission, without showing variations based on the individual performing the task. These findings highlight the potential of cell morphology as a highly accurate and effective biomarker for CNS infections. 3D holotomography provides real-time, label-free, and cost-effective imaging of cell morphology. [11] While recent studies utilizing genomic analysis of CSF immune cells have enabled the identification of molecular pathways and gene expression changes underlying inflammatory responses in patients with CNS infections, our approach offers distinct advantages in terms of cost-effectiveness, real-time analysis, and morphologically interpretable information. [8–12]

Even in multiclassification, the deep-learning model leveraging the cell structure performed well. In the future, it might be feasible to classify the different etiologies that were not covered in this study. Viral infections, particularly those from the herpes virus family and enteroviruses, are the most frequent causes of CNS infections. [22] From our cohort, we isolated patients with Herpesviridae and performed individual classifications. The model showed respectable performance, with AUROC > 0.86. Even in infections caused by the same viral family, immune responses may vary depending on the specific subtypes.<sup>[23]</sup> This study highlighted the possibility of identifying these differences. Previously published prognostic prediction studies were confined to specific situations. [20,24-26] However, our study used CSF data obtained from patients in the early stages of admission, without being limited to specific scenarios. Furthermore, our AI model does not require the identification of the cause, which makes it particularly helpful in primary care settings.

In this study, the DenseNet model achieved an AUROC of 0.89, demonstrating superior diagnostic discrimination performance compared to the ResNet model, which achieved an AUROC of 0.82. This performance difference is likely due to DenseNet's architecture, which concatenates features from all preceding layers rather than relying on skip connections like ResNet.<sup>[27]</sup> This enhances feature reuse, gradient flow, and robustness, particularly in tasks requiring fine-grained feature extraction.<sup>[28]</sup> These advantages extend to cell morphology image classification, as demonstrated in a previous study on RBC morphology, where the DenseNet-121 model outperformed the

ResNet-50 model in accuracy. [29] Similarly, our modified 3D DenseNet-169 likely exhibited greater resistance to overfitting and improved gradient flow compared to 3D ResNet-101, contributing to its superior performance in 3D cellular image classification. For the AI explainability, we used the Grad-CAM algorithm, in addition to applying deep learning to create a predictive model. Grad-CAM is a technique that visualizes which part of the image the model focuses on when making predictions, allowing us to observe the concentration in the interior of cells, particularly the nucleus. When we analyzed the cells on a shell-by-shell basis, we observed a rapid decrease in RI density toward the outer regions in patients with a viral infection, accompanied by an overall increase in nuclear components. This pattern is believed to be associated with the focus on the interior of the cells in Grad-CAM. Cells with active immune responses exhibit a distribution of cellular structures across the entire cell, showing a pattern of cell expansion and gradual decrease in density as they move peripherally.<sup>[7,30]</sup> This pattern has been observed in patients with bacterial infections and tuberculosis. Interestingly, when analyzed on a shell-by-shell basis, even in the group with poor prognosis at discharge, a pattern similar to that of the nonviral group was observed. This suggests that changes in the internal structure of the immune cell driven by early immune responses may be linked to patient prognosis.

Depending on the source of infection, phenomena such as monocyte vacuolization, atypical lymphocytes, and myeloid shifts can occur. [7,31] However, infection-related morphological changes in immune cells have not been fully studied previously. [6,7] Particularly in the CSF, where cells are naturally less abundant, unlike in the blood, little is known about structural changes in the immune cells during inflammation.<sup>[5]</sup> Recent genomic studies revealed the role of the immune cells within the CSF in various brain disorders, including neurodegenerative conditions.<sup>[8,9,32,33]</sup> Morphological changes in the CSF immune cells in acute and infectious brain disorders were the basis of our research, and we found that the structure of these cells could vary depending on the invading pathogen. This information can be used for prognostication. Future studies based on genomic analysis may help identify biomarkers for a wide range of brain disorders.

# 4. Limitation

The present study had some limitations. First, the small sample size may have led to sampling bias, while precluding detailed analysis based on pathogen type. Second, this study was conducted at a single center; thus, external validation could not be performed. Third, holotomography used to analyze cellular morphological features does not provide molecular-level information, such as RNA or DNA. While this study primarily focuses on the novel contributions of cell morphology, we recognize the potential for integrating genomic and morphological data in future research to establish a more comprehensive multi-modal framework. Therefore, we plan to explore potential quantitative comparisons within a well-defined experimental scope that allows for a meaningful evaluation of both modalities. Finally, because most individuals included in this study were of Asian

www.advancedsciencenews.com www.advintellsyst.com

ethnicity, there may be variations when the findings are applied to patients of other ethnicities.

#### 5. Conclusion

This study represents the first attempt at utilizing the 3D morphological features of immune cells in the CSF and a deeplearning model for the diagnosis and prognosis prediction of patients with CNS infections. In this AI-driven study, we applied various techniques to clarify and explain our results. The presented findings may shorten the time required for the diagnosis and prognosis prediction if applied in clinical practice. This study will help improve patient outcomes by rapidly providing customized therapy.

# 6. Experimental Section

CSF Sample Preparation: The CSF samples obtained through lumbar puncture were stored in a BD Vacutainer Urinalysis Tube 364979 (Becton Dickinson, Franklin Lakes, NJ, USA) and kept refrigerated at 4 °C. The sample was centrifuged at 400  $\times$  g for 5 min at room temperature (22-24 °C). The plasma layer was carefully separated, and the pellet was resuspended in phosphate-buffered saline using a sterile Pasteur pipette.

Cell Image Acquisition and Preprocessing: All 3D cell structural images of the immune cells in the CSF were captured using 3D holotomography (HT-2H; Tomocube Inc., Daejeon, Republic of Korea). This technology reconstructed 3D RI portrayals by merging various 2D quantitative phase images.<sup>[34]</sup> Cellular RI served as an inherent optical parameter that dictates the trajectory of light traversing the cell matrix, as evidenced by physical phenomena such as light scattering and absorption. As a result, RI was closely associated with the quantity and dispersion of cellular mass. [11] Our preprocessing methods involved the manual exclusion of subpar instances (encompassing low-quality, low-resolution, and noisy backdrop depictions), as well as images exhibiting excessive adjacency of two or more cells. Through this process, 463 images were excluded from the initial set of 1,890 images, resulting in 1427 images being used for training.

The following preprocessing steps were performed after the image selection. The morphological form of each cell was determined using a predetermined threshold. After the acquisition, each 3D cell image was subjected to a center-cropping process to a size of  $64\times64\times64$  pixels and centered around the morphological center co-ordinates determined manually during the previous curation process.

Quantitative Analysis of Cell Morphology: The quantitative features of each cell structure were calculated from independent label-free 3D cell images. First, a binary mask was created to segment the cells in the background by applying a predefined threshold RI. Subsequently, the cell volume (fL) was determined based on the number of voxels corresponding to the interior of the cell. Protein density (g dL<sup>-1</sup>) was calculated by summing the differences between the RI of individual voxels within the cell and the medium RI value, followed by multiplying the sum by 500. The calculated protein density was multiplied by the cell volume and divided by 100 to obtain the dry mass (pg).

Deep-Learning Model Development for Etiological Classification: A deeplearning model for identifying the pathogen and predicting the prognosis of CNS infections was developed based on 3D cell images of each cell. All models were built by receiving 3D RI tomogram images as inputs and outputting the final predictions. The dataset was divided into training, validation, and test sets at a ratio of 8:1:1.

The model architecture was derived from a modified DenseNet, which had been utilized in previous research.<sup>[35]</sup> To train the model, we implemented a cross-entropy loss function and utilized a stochastic gradient descent algorithm with 8 minibatch sizes of 8. We employed the cosine annealing technique without restarts to dynamically adjust the learning

Adv. Intell. Syst. 2025, 7, 2401145

rate, initially setting it to 0.0001 and altering it over a span of 128 epochs. As the cosine annealing technique rapidly increases and then decreases the learning rate with cosine function between the maximum and minimum values, this enables the model to quickly escape saddle points in the manifold space of the model and maximizes the generalizability of the model. To prevent model overfitting, data augmentation, drop-out, and early stopping methods were incorporated into the training process. Data augmentation involved several transformations, including random rotations, horizontal flips, and vertical flips, which were applied to each image once in every epoch to diversify the training dataset. The dropout rate was set to 0.5. The early stopping mechanism monitored the model's performance by evaluating the validation loss, and the training was terminated if no improvement was observed within the patience window of 15 epochs. For class imbalance, we used class weights. We evaluated all models using 10-fold cross validation, and the overall performance was measured using the AUROC, accuracy, and F1 score. During the AUROC calculation, we estimated the corresponding 95% CI obtained through 1000 bootstrapping iterations. The Grad-CAM algorithm was applied to confirm the visual expansion of the proposed deep-learning model by checking the area where the model was focused locally for each image.

The entire deep-learning process was conducted using PyTorch version 1.12.1 (Meta Al, Astor Place, NY, USA) and Python version 3.9.12 (Python Software Foundation, Beaverton, OR, USA). The entire process was executed on a server equipped with two Quadro RTX 8000 GPUs (Nvidia Corp., Santa Clara, CA, USA), each with 48 GB of memory, and operated on CUDA version 11.6 (Nvidia Corp.) to accelerate computations.

Cellular Shell Segmentation and Spatial Distribution: We extracted the cross-sectional images by segmenting each cell region based on the center co-ordinates set earlier and divided the cell into eight elliptical shell regions. We calculated the Euclidean distances from the center of the cell to every voxel, resulting in a ranked list ranging from the nearest to the farthest voxels. This ranked list was then evenly divided into eight segments, each of which was assigned a unique shell. Shell 1 represented the innermost domain, whereas shell 8 occupied the outermost territory. This subdivision strategy ensured an equitable distribution of voxels across each shell, generating eight discrete subregions within each cell. Following segmentation into shells, each shell was transformed into a binary mask. Subsequently, we applied a lower-intensity threshold to the original image to enhance the visibility of the cellular structures while reducing the background noise. The next step involved multiplying the binary mask of each shell by the original image, resulting in a shell-specific image. This process selectively highlighted the voxels within each specific shell, setting all others to "0" for precise differentiation. To determine the density of each shell, we tabulated the count of nonzero voxels and divided this image by the total number of voxels within that specific shell. The example images of the segmented cell images into shell units and their distribution of the refractive index values are visualized in Figure S6, Supporting Information.

Statistical Analysis: The patients' demographic and clinical characteristics were summarized for the entire cohort at the patient level. Categorical variables are expressed as frequencies and percentages, and continuous variables as medians with interquartile ranges. The quantified features of cell morphology were continuous variables, and independent t-tests were used for comparisons between the groups. To compare the spatial distribution within the cells, the RI density of each shell component was compared between groups using an independent t-test.

All statistical analyses were performed using R, version 4.11 (R foundation for Statistical Computing, Vienna, Austria). Two-sided p-values < 0.05 were considered indicative of statistical significance.

# **Supporting Information**

Supporting Information is available from the Wiley Online Library or from the author.

www.advancedsciencenews.com



www.advintellsyst.com

# **Acknowledgements**

YRP was supported by the Hyundai Motor Chung Mong-Koo Foundation. BKC was supported by the MD-PhD/Medical Scientist Training Program through the Korea Health Industry Development Institute (KHIDI). We would like to express our sincere gratitude to Tomocube Inc. for their invaluable support.

#### Conflict of Interest

The authors declare no conflict of interest.

#### **Author Contributions**

Bo Kyu Choi: conceptualization (equal); data curation (equal); formal analysis (lead); investigation (lead); methodology (equal); software (supporting); validation (lead); visualization (supporting); writing-original draft (lead); writing-review and editing (equal). Ho Heon Yang: formal analysis (supporting); software (supporting); validation (supporting); visualization (lead); writing—original draft (supporting). Jong Hyun Kim: conceptualization (supporting); data curation (supporting); formal analysis (supporting); investigation (supporting); software (equal); visualization (supporting); writing-original draft (supporting). JaeSeong Hong: data curation (supporting); investigation (supporting); software (equal); writing—review and editing (supporting). Kyung Min Kim: conceptualization (supporting); data curation (lead); investigation (supporting); methodology (supporting); supervision (equal); validation (equal); writing-review and editing (lead). Yu Rang Park: conceptualization (lead); funding acquisition (lead); investigation (supporting); methodology (equal); project administration (lead); resources (lead); supervision (equal); writing-review and editing (lead). Kyung Min Kim and Yu Rang Park contributed equally to this work.

## **Data Availability Statement**

Research data are not shared

#### **Keywords**

artificial intelligence, deep learning, encephalitis, holotomography, meningitis, neuroinflammation

Received: December 28, 2024 Revised: March 9, 2025 Published online: March 26, 2025

- [1] H. Erdem, A. Inan, E. Guven, S. Hargreaves, L. Larsen, G. Shehata, E. Pernicova, E. Khan, L. Bastakova, S. Namani, A. Harxhi, T. Roganovic, B. Lakatos, S. Uysal, O. R. Sipahi, A. Crisan, E. Miftode, R. Stebel, B. Jegorovic, Z. Fehér, C. Jekkel, N. A. Moravveji, H. Yilmaz, A. Khalifa, U. Musabak, S. Yilmaz, A. Jouhar, N. Oztoprak, X. Argemi, et al., Eur. J. Clin. Microbiol. Infect. Dis. 2017, 36, 1595.
- [2] J. Granerod, H. E. Ambrose, N. W. S. Davies, J. P. Clewley, A. L. Walsh, D. Morgan, R. Cunningham, M. Zuckerman, K. J. Mutton, T. Solomon, K. N. Ward, M. P. T. Lunn, S. R. Irani, A. Vincent, D. W. G. Brown, N. S. Crowcroft, Lancet Infect. Dis. 2010, 10, 835.
- [3] A. Bhimraj, R. Hasbun, Curr. Opin. Infect. Dis. 2022, 35, 231.
- [4] S. Mintegi, S. García, M. J. Martín, I. Durán, E. Arana-Arri, C. L. Fernandez, J. Benito, S. Hernández-Bou, *Pediatrics* 2020, 146, 1126.

- [5] F. Otto, C. Harrer, G. Pilz, P. Wipfler, A. Harrer, Diagnostics 2021, 12, 79.
- [6] Y. German, L. Vulliard, A. Kamnev, L. Pfajfer, J. Huemer, A. K. Mautner, A. Rubio, A. Kalinichenko, K. Boztug, A. Ferrand, J. Menche, L. Dupré, Cell Rep. 2021, 36, 109318.
- [7] Y. Severin, B. D. Hale, J. Mena, D. Goslings, B. M. Frey, B. Snijder, Sci. Adv. 2022, 8, eabn5631.
- [8] M. Heming, X. Li, S. Räuber, A. K. Mausberg, A. L. Börsch, M. Hartlehnert, A. Singhal, I. N. Lu, M. Fleischer, F. Szepanowski, O. Witzke, T. Brenner, U. Dittmer, N. Yosef, C. Kleinschnitz, H. Wiendl, M. Stettner, G. Meyer zu Hörste, *Immunity* 2021, 54, 164.
- [9] D. Schafflick, C. A. Xu, M. Hartlehnert, M. Cole, A. Schulte-Mecklenbeck, T. Lautwein, J. Wolbert, M. Heming, S. G. Meuth, T. Kuhlmann, C. C. Gross, H. Wiendl, N. Yosef, G. Meyer zu Horste, Nat. Commun. 2020, 11, 247.
- [10] T. L. Nguyen, S. Pradeep, R. L. Judson-Torres, J. Reed, M. A. Teitell, T. A. Zangle, ACS Nano 2022, 16, 11516.
- [11] J. Park, B. Bai, D. Ryu, T. Liu, C. Lee, Y. Luo, M. J. Lee, L. Huang, J. Shin, Y. Zhang, D. Ryu, Y. Li, G. Kim, H. Min, A. Ozcan, Y. Park, Nat. Methods 2023, 20, 1645.
- [12] Y. J. Jo, H. Cho, W. S. Park, G. Kim, D. H. Ryu, Y. S. Kim, M. Lee, S. Park, M. J. Lee, H. Joo, H. H. Jo, S. Lee, S. Lee, H. Seok Min, W. Do Heo, Y. K. Park, *Nat. Cell Biol.* **2021**, *23*, 1329.
- [13] J. Rankin, Scott. Med. J. 1957, 2, 200.
- [14] A. Mlinarić, Ž. Vogrinc, Z. Drenšek, Biochem. Med. 2018, 28, 030705.
- [15] A. P. Hrishi, M. Sethuraman, Indian J. Crit. Care Med. 2019, 23, S115.
- [16] A. Venkatesan, B. Jagdish, Semin. Neurol. 2019, 39, 312.
- [17] D. Velissaris, M. Pintea, N. Pantzaris, E. Spatha, V. Karamouzos, C. Pierrakos, M. Karanikolas, J. Clin. Med. 2018, 7, 148.
- [18] H. O. Peltola, The Lancet 1982, 319, 980.
- [19] D. Babenko, A. Seidullayeva, D. Bayesheva, B. Turdalina, B. Omarkulov, A. Almabayeva, M. Zhanaliyeva, A. Kushugulova, S. Kozhakhmetov, *Biomed Res. Int.* 2021, 2021, 5519436.
- [20] B. S. Park, S. E. Kim, S. H. Park, J. Kim, K. J. Shin, S. Y. Ha, J. S. Park, S. E. Kim, B. I. Lee, K. M. Park, J. Clin. Neurosci. 2017, 36, 129.
- [21] E. Guzmán, M. V. Belmonte, V. M. Lelis, Expert Syst. 2022, 39, e12996.
- [22] S. Li, I. P. Nguyen, K. Urbanczyk, Quant. Imaging Med. Surg. 2020, 10, 2227.
- [23] S. Ahmed, P. van Zalm, E. A. Rudmann, M. Leone, K. Keller, J. A. Branda, J. Steen, S. S. Mukerji, H. Steen, Viruses 2022, 14, 2757.
- [24] K. T. Thakur, M. Motta, A. O. Asemota, H. L. Kirsch, D. R. Benavides, E. B. Schneider, J. C. McArthur, R. G. Geocadin, A. Venkatesan, *Neurology* 2013, 81, 793.
- [25] Y. Zhang, Q. Zeng, Y. Fang, W. Wang, Y. Chen, Ther. Innov. Regul. Sci. 2022, 56, 651.
- [26] G. Lu, Y. Liu, Y. Huang, J. Ding, Q. Zeng, L. Zhao, M. Li, H. Yu, Y. Li, J. Hosp. Infect. 2023, 136, 90.
- [27] G. Huang, Z. Liu, L. Van Der Maaten, K. Q. Weinberger, in Proc. 2017 IEEE Conf. on Computer Vision and Pattern Recognition, IEEE, Honolulu, HI 2017, p. 2261.
- [28] C.-Y. Lee, S. Xie, P. Gallagher, Z. Zhang, Z. Tu, in *Proc. 18th Int. Conf. Artificial Intelligence Statistics*, PMLR, San Diego, California 2015, pp. 562–570.
- [29] K. Pasupa, S. Vatathanavaro, S. Tungjitnob, J. Ambient Intell. Humaniz. Comput. 2023, 14, 15259.
- [30] K. W. Keohane, W. K. Metcalf, *Nature* **1959**, *183*, 195.
- [31] O. Pozdnyakova, N. T. Connell, E. M. Battinelli, J. M. Connors, G. Fell, A. S. Kim, Am. J. Clin. Pathol. 2021, 155, 364.

www.advancedsciencenews.com

www.advintellsyst.com

- [32] N. Piehl, L. van Olst, A. Ramakrishnan, V. Teregulova, B. Simonton, Z. Zhang, E. Tapp, D. Channappa, H. Oh, P. M. Losada, J. Rutledge, A. N. Trelle, E. C. Mormino, F. Elahi, D. R. Galasko, V. W. Henderson, A. D. Wagner, T. Wyss-Coray, D. Gate, Cell 2022, 185, 5028.
- [33] A. Yekula, J. Tracz, J. Rincon-Torroella, T. Azad, C. Bettegowda, Brain Sci. 2022, 12, 812.
- [34] Y. K. Park, C. Depeursinge, G. Popescu, Nat. Photonics 2018, 12, 578.
- [35] G. Kim, D. Ahn, M. Kang, J. Park, D. H. Ryu, Y. J. Jo, J. Song, J. S. Ryu, G. Choi, H. J. Chung, K. Kim, D. R. Chung, I. Y. Yoo, H. J. Huh, H. S. Min, N. Y. Lee, Y. K. Park, Light Sci. Appl. 2022, 11, 190.

Adv. Intell. Syst. 2025, 7, 2401145